Received: 15 January 2021 | Revised: 24 March 2021 | Accepted: 18 April 2021

DOI: 10.1111/jace.17863

Journal of the American Ceramic Society

ORIGINAL ARTICLE

Cold sintering of diatomaceous earth

Anna Galotta | Enrico Giust | Mauro Bortolotti | Gian D. Sorarù | Vincenzo M. Sglavo | Mattia Biesuz

Department of Industrial Engineering, University of Trento, Trento, Italy

Correspondence
Mattia Biesuz, Department of Industrial Engineering, University of Trento, Via Sommarive 9, 38123 Trento, Italy.
Email: mattia.biesuz@unitn.it

Funding information
Ministero dell'Istruzione, dell'Università e della Ricerca, Grant/Award Number: 2017FCFYHK and 2017PMR932

Abstract

Diatomite, a natural silicate-based sedimentary rock, was densified by cold sintering at room temperature and 150°C under various pressures (100, 200, and 300 MPa) and using different NaOH water solutions (0–3 M). The relative density of cold sintered diatomite can be as high as 90%, a condition that can be achieved by conventional firing only at 1200–1300°C. The cold sintered materials maintain the same mineralogical composition of the starting powder (quartz, glass, and illite) and are constituted by well-deformed and flattened grains oriented orthogonally to the applied pressure. Conversely, an evident phase evolution takes place upon conventional firing with the formation of cristobalite and mullite. The bending strength of cold sintered artifacts can exceed 40 MPa and increases to ≈80 MPa after post-annealing at 800°C, such mechanical strength is much larger than that of conventionally pressed samples sintered at 800°C, which is only ≈1 MPa.

KEYWORDS

cold sintering, diatomite, silicate minerals, sintering, solubility

1 | INTRODUCTION

The increasing awareness about global warming and climate change urges the development of novel techniques able to reduce the carbon footprint of the ceramic industry.[1,2] In the present research context, the cold sintering process (CSP) is gaining increasing interest as it allows near room temperature (RT) consolidation of several ceramic systems.[3–7] CSP is a liquid-assisted technology where the addition of water (or alternative solvent) combined with external pressure (from a few tens to a few hundreds of megapascals) allows sintering ceramic artifacts in "warm" conditions (i.e., typically below 350°C). CSP is an evolution of hot hydrothermal pressing (HHP) developed during the 1980 s in Japan,[8–10] but it uses much simpler and inexpensive facilities. A typical CSP consists of the following steps: (i) the ceramic powder is mixed with a solvent to produce a paste that is (ii) introduced in a mold (die/punches) and (iii) pressed. The process is carried out at near RT and the die/punches assembling is not sealed thus allowing water evaporation. Despite the mainstream in the CSP scientific community[6] is that the process is fundamentally based on liquid phase sintering (LPS), originating from dissolution/reprecipitation phenomena, recent experimental and theoretical works seem to suggest that additional mechanisms could be relevant such as water-induced plastic or viscous flow.[11–15]

The first materials produced by CSP were mainly salts and soluble compounds,[3,16] although several activities have been then carried out on ferroelectrics,[16–18] piezoelectrics,[19] magnetic ceramics,[20] semiconductors,[21–23] transparent ceramics,[24] bioceramics,[14] and ionic conductors.[25–27] More recent works regard water-assisted cold processing of silicate ceramics including cold sintering of quartz,[28] soda-lime silicate glass,[15] and quartz-PTFE composite[29] or cold joining of silica[30] and cold isotactic pressing of glass monoliths.[31]

Although CSP is inspired by phenomena taking place in nature (like the formation of sedimentary rocks[32]), no research activities regarding the application of CSP on nonsynthetic industrial minerals have been reported to the best of the authors' knowledge.

In the present work, the cold sintering of diatomaceous earth, or simply diatomite, was investigated. Diatomite is a silicate-based material constituted by the skeleton (frustules) of diatoms, eukaryotic unicellular microalgae. Deposits of diatomite can be found worldwide as sedimentary rocks.[33] Frustules are made of various self-assembled bio-silica architectures forming a highly porous pattern ranging from the microscale to the nanoscale.[34] The resulting structure is responsible for diatomite physical–chemical properties like high surface area, thermal stability, and good chemical and mechanical resistance.[35]

The abundance, low-price, and unique properties of this material are the reasons why diatomite has been widely used in many technical fields including thermal insulation,[36] constructions, catalysis, filters, hazardous waste absorption,[37] paint fillers, and insecticide.[38]

Herein, we studied the cold sintering process of diatomaceous earth aiming at (i) pointing out the applicability of CSP to such material, (ii) understanding the effect of the main process conditions (pressure, temperature, liquid solution composition) on densification, and (iii) identifying the microstructural features of the CSP material. The microstructural evolution of the CSP products is also compared with that obtained by conventional sintering. To point out whether cold sintering allows a "proper sintering" of the material with strong interparticle bonding, a preliminary mechanical characterization was carried out on the densest samples.

2 | EXPERIMENTAL PROCEDURES

2.1 | Samples preparation

Commercially available diatomite powder was provided by a Vietnamese mineral joint-stock company in Phu Yen. The powder was dried overnight before being used.

About 0.4 g of diatomite powders were uniaxially pressed at 100 MPa by a hydraulic manual press (Specac) in a cylindrical die (ø = 13 mm) (Specac) to prepare the samples for conventional sintering (CS). This was carried out in Nabertherm P330 muffle furnace with a heating rate of 10°C min^{-1} and 1 h holding time at the sintering temperature, varied between 800°C and 1300°C.

Pellets for cold sintering were produced by mixing 0.4-g powder with 0.25-g NaOH (Sigma Aldrich) water solution with four different concentrations (0, 0.1, 0.5, 1, and 3 M). The obtained mix, whose consistency is that of a paste, was introduced into a cylindrical die (ø = 13 mm) and pressed using a mechanical testing machine (MTS 810, Material Test System). Three pressure levels were applied (100, 200, and 300 MPa) with a ramp of 15 kN min^{-1}. Once the maximum pressure was reached, the mold was heated up to 150°C using a heating ring wrapped around the die. Maximum temperature and pressure were held constant for 12 min. Three specimens (one for each pressure level) were also cold sintered at RT by mixing the diatomite powder with a 3-M NaOH water solution. The samples cold sintered at RT were dried at 150°C for 15 min before being characterized.

Finally, some samples cold sintered at 150°C using 3-M NaOH solution and 300 MPa were post-annealed at 800°C for 1 h (heating rate = 3°C min^{-1} up to 600°C, 10°C min^{-1} up to 800°C).

2.2 | Materials characterization

The chemical composition of diatomite powders was determined by ICP-AES. The powders were dissolved in molten lithium tetraborate at 1050°C in a Pt crucible. The melt was then quenched and dissolved in nitric acid solution HNO_3 (4%) for 2 h, and then 2-ml HF were added. The analyses were carried out with a normal torch, adding 1-ml boron oxide water solution (30 g L^{-1}) every 9-ml nitric acid solution. The product was therefore analyzed by a Spectro Ciros instrument (Spectro Analytical Instruments GmbH & Co).

Infrared Attenuated Total Reflectance (IR-ATR) spectroscopy was carried out to access the chemical bonds of diatomite raw material and sintered specimens. All spectra were collected from 4000 to 600 cm^{-1} using a Spectrum One spectrometer (Perkin Elmer).

Mineralogical phases were determined by X-ray diffraction (XRD) (Italstructures, IPD 3000). The diffractometer was equipped with a Co-Kα (λ = 1.7902 Å) X-ray source excited at 40 kV, 30 mA. Once collected, the XRD spectra were analyzed by MAUD® software, based on the Rietveld refinement.

The thermal evolution of the raw material was studied by thermogravimetric analysis (TGA) and differential thermal analysis (DTA) up to 1350°C with a NETZSCH Geraerebau GmbH STA 409 thermobalance (heating rate = 20°C min^{-1}). Moreover, the linear shrinkage was evaluated up to 1350°C using an L75 PT horizontal dilatometer (Linseis) using a heating rate equal to 20°C min^{-1}. Dilatometric test was carried out on a cylindrical sample (diameter = 13 mm, height = 4 mm) produced by uniaxial pressing the raw powder at 100 MPa. The pressure applied by the dilatometer piston on the sample was about 4 kPa.

The microstructural evolution was analyzed by scanning electron microscopy (SEM) (JEOL JSM-5500). Micrographs were acquired on the raw material and the fresh fracture surface of sintered samples. Powder and sintered samples were preliminarily made conductive with a Pd–Pt sputter coating.

The density of conventionally sintered pellets was measured by Archimedes' method using distilled water as immersing medium while only the bulk density was determined for cold sintered materials to avoid any possible reactions between water and soda-rich glass. The density measurements were carried out using an analytical balance (Gibertini) and a digital caliper with sensitivity 0.1 mg and 0.01 mm, respectively. The theoretical density of the cold sintered bodies was determined on the milled artifacts by He picnometry (AccuPyc 1330 TC, Micromeritics). The open porosity of the diatomite loose powder and of the densest cold sintered sample was evaluated by Hg porosimetry, the analysis being carried out using a Porosimeter 2000 (Carlo Erba).

Starting from the data collected with the mechanical testing machine (time, displacement, and load) during cold sintering, temperature measurements, and the final density of the sintered bodies, the density evolution upon CSP was estimated as a function of time and temperature. The displacement raw data were corrected by subtracting the contribution of the die and mechanical testing machine deformation and the thermal expansion. This was determined by carrying out the tests with an empty die and the same conditions (temperature, pressure, and heating/pressing rate).

The biaxial flexural strength was measured on the samples (i) conventionally sintered at 800°C, (ii) cold sintered at 150°C (3-M NaOH solution, 300 MPa), and (iii) cold sintered at 150°C (3-M NaOH solution, 300 MPa) + post-annealing at 800°C. The piston-on-three-balls test was carried out using an MTS 810 mechanical testing machine equipped with a 5-kN load cell and using the ISO 6872:15 standard as a reference. The sample (diameter ≈13 mm) was placed on three supporting balls, equally spaced at 120°C, and loaded by a steel piston (2-mm diameter) moving at 0.5 mm s^{-1}.

The biaxial flexural strength was determined as[39]

$$\sigma_{\text{bfs}} = \frac{-0.2837P\,(X-Y)}{s^2}, \tag{1}$$

where

$$X = (1+\nu)\ln\left(\frac{r^2}{R^2}\right) + \left(\frac{1-\nu}{2}\right)\left(\frac{r^2}{R^2}\right), \tag{1a}$$

$$Y = (1+\nu)\left[1+\ln\left(\frac{a^2}{R^2}\right)\right] + (1-\nu)\left(\frac{a^2}{R^2}\right), \tag{1b}$$

P being the failure load, s the sample thickness, ν the Poisson ratio (assumed equal to 0.2 as intermediate between fused silica, 0.17,[38] and soda-lime silicate glass, 0.22[40]), r the radius of the piston, R the radius of the sample, and a the radius of the circle generated by the supporting spheres. The strength was determined as an average over at least five measures.

3 | RESULTS AND DISCUSSION

The diatomite powder used in the present work is mainly constituted by the fossilized diatom shells, and its size ranges from a few microns to several tens of microns (Figure 1). The chemical composition in terms of metallic elements as determined by ICP-AES is (wt%) as follows: 61.0 Si, 19.9 Al, 9.4 Fe, 5.5 K, 1.3 Mg, 1.2 Na, 0.9 Ca, 0.8 Ti, 0.1 others. The XRD analysis of the powder revealed the presence of three main phases (Figure 2A): α-quartz (ICDD/PDF 46-1045), illite (ICDD/PDF 29/1496), and silicate glass, as evidenced by a broad hump around $2\theta \approx 25°$C. The abundant presence of a clay mineral (i.e., illite) is consistent with the results of the ICP-AES analysis, which revealed that Al is the second most abundant metal; furthermore, being illite typically highly substituted in nature, it also accounts for the significant amount of Fe, Mg, K, Ca, and Ti.

The Fourier transform infrared (FTIR) spectrum (Figure 2B) recorded on the diatomite powder is characterized by two well-defined peaks, one at 1048 cm^{-1}, due to the asymmetric stretching of siloxane (Si–O–Si) groups,[41,42] and another at 798 cm^{-1}, which can be assigned both to symmetric stretching of Si–O[43,44] as well as to Al–O–Si stretching,[43,45] this being consistent with the presence of illite.

As said, cold sintering was carried out on diatomite powder mixed with sodium hydroxide (NaOH) water solutions. The solubility rate for silicon dioxide is strongly affected by the solution pH,[46] and it increases by about two orders of magnitude changing from acid to basic solutions.[47] Furthermore, the solubility strongly increases with temperature; that is, by heating the system from RT to 65°C, SiO_2

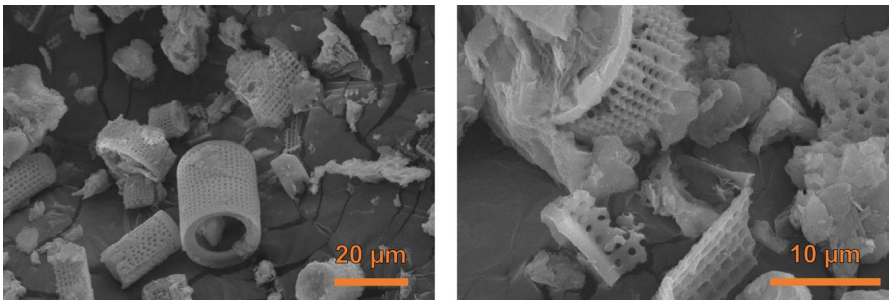

FIGURE 1 Scanning electron microscopy micrographs of the diatomite powder [Color figure can be viewed at wileyonlinelibrary.com]

solubility grows by three orders of magnitude.[47] In agreement with such background, alkaline solutions have been already used for cold sintering quartz,[28] quartz-PTFE composites,[29] silicate glasses,[15] and silicate-based materials like zeolite Y.[48]

No phase transformations were detected during CSP, independently from the water solution concentration, applied pressure, and temperature: only quartz, amorphous silicate glass (probably including NaOH solution residue), and illite are detected by the XRD spectra, as shown in Figure 2A. These results point out that CSP allows to maintain the starting powder structure during the densification process. It appears therefore an effective tool for the consolidation of metastable phases that could undergo thermal transformation upon sintering.

Figure 2B shows the FTIR spectra of cold sintered materials. The stretching signals at about 1040–1020 cm^{-1} and 798–796 cm^{-1} are always present. A weak red-shift of the Si–O–Si peak can also be appreciated in the CSP samples revealing a modification of the structural order of SiO_2 and the variation of the bond angles due to nonbridging oxygens formation. As a matter of fact, nonbridging oxygens are expected to form through the reaction between silica and NaOH.[49] An additional peak is visible at 1634–1637 cm^{-1} in cold sintered diatomite and can be associated with bending of OH groups of water.[43] A weak and broad feature at about 3500 cm^{-1} can also be detected; it is associated with OH stretching.[43]

Differently from CSP materials, the samples prepared via conventional sintering show evident structural/mineralogical alterations if compared with the raw powder. According to the TGA analysis (Figure 3A), raw diatomite undergoes a weight loss of about 2% at ≈100°C upon firing due to the removal of absorbed humidity. Other two weight losses of ≈0.5 wt% can be observed at 470°C–550°C and 650°C–870°C, these being related to clay dihydroxylation.[50,51] The results are further confirmed by the DTA analysis, which shows an extended endothermic phenomenon between 470°C and 900°C. The dilatometric curve recorded on the raw powder pellet (Figure 3B) is characterized by two shrinkages with maximum intensity at 930°C and 1185°C: the former corresponds to a modest linear shrinkage of ≈2.5%, whereas the latter leads to a linear contraction exceeding 20%.

XRD pattern corresponding to the raw powder and to the conventionally sintered samples (Figure 4A) does not change significantly between RT and 800°C, the sample sintered at such temperature still containing quartz, silicate glass, and illite (note that hydrated and anhydrous illite possess very similar crystal structures, which make them substantially indistinguishable[52,53]). At 900°C, illite starts to decompose, and also quartz partially dissolves in the glassy phase. At 1000°C, illite peaks completely disappear and the material fundamentally contains amorphous silica and quartz relicts. Starting from 1100°C, cristobalite (ICDD/PDF 39-142) and mullite (ICDD/PDF 15-776) crystallize from the

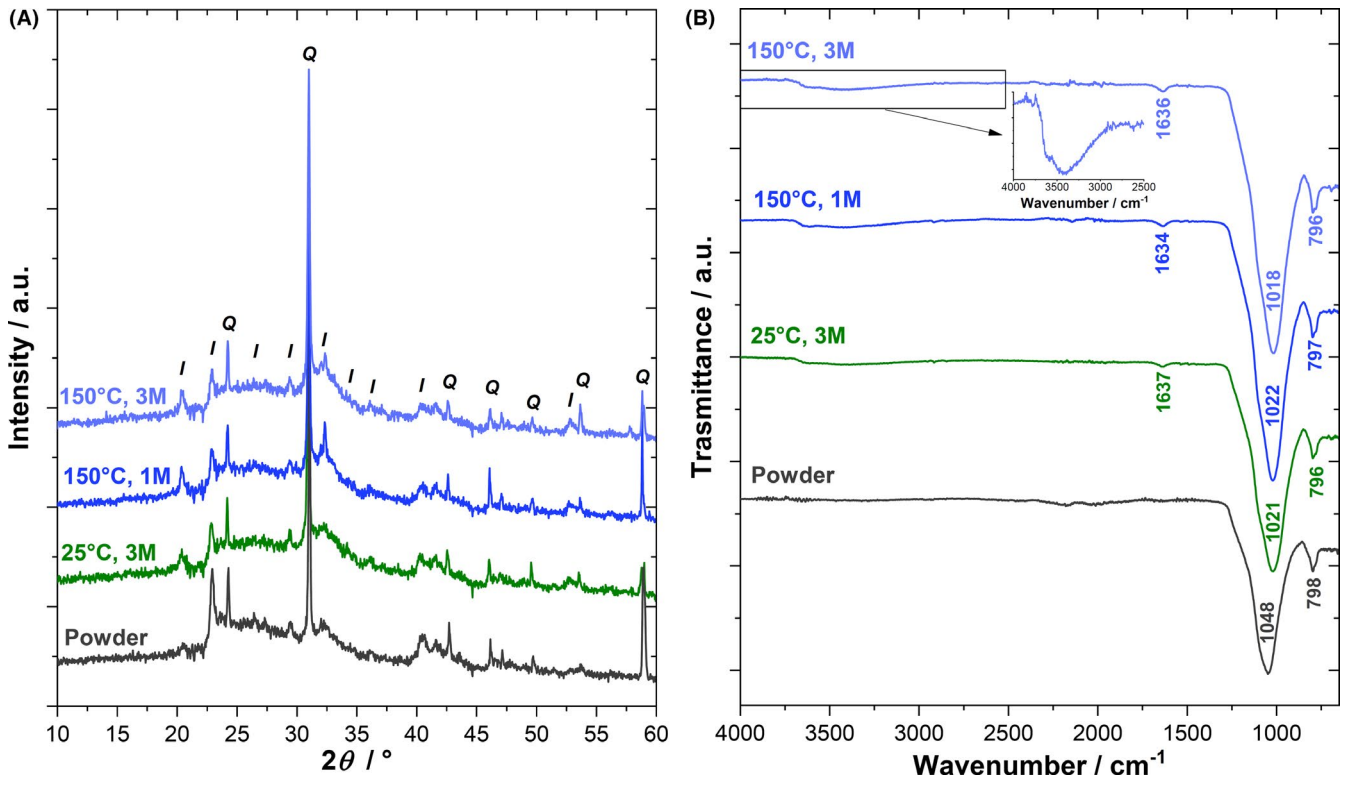

FIGURE 2 X-ray diffraction (A) and Fourier transform infrared (B) spectra of cold sintering process specimens. The phases in (A) are identified as: Q = quartz, I = illite [Color figure can be viewed at wileyonlinelibrary.com]

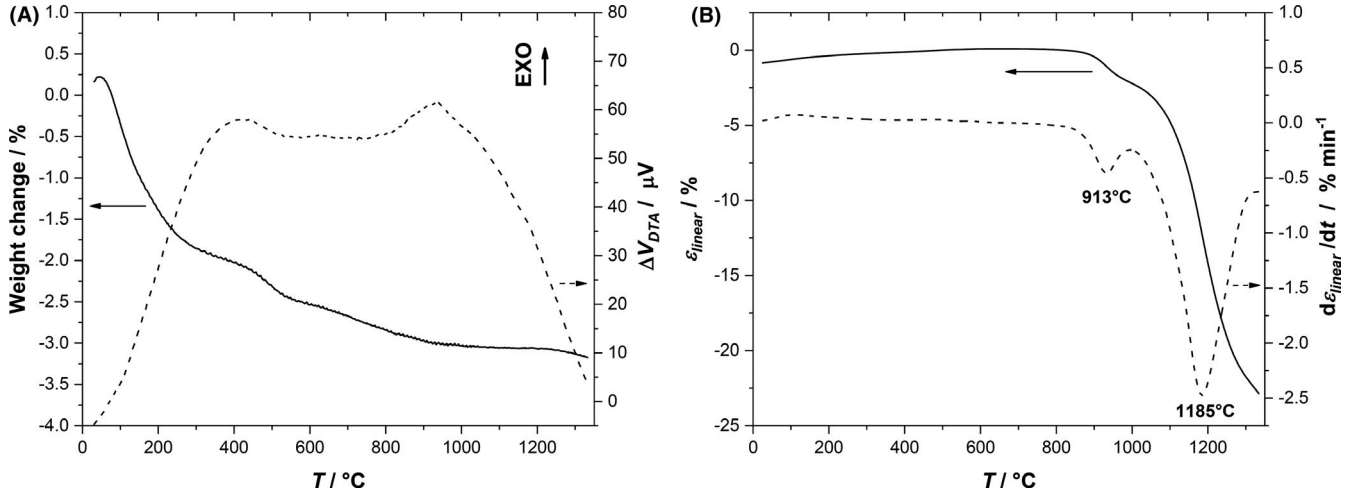

FIGURE 3 Thermal analysis of diatomite powder: (A) thermogravimetric analysis–differential thermal analysis and (B) dilatometric curves

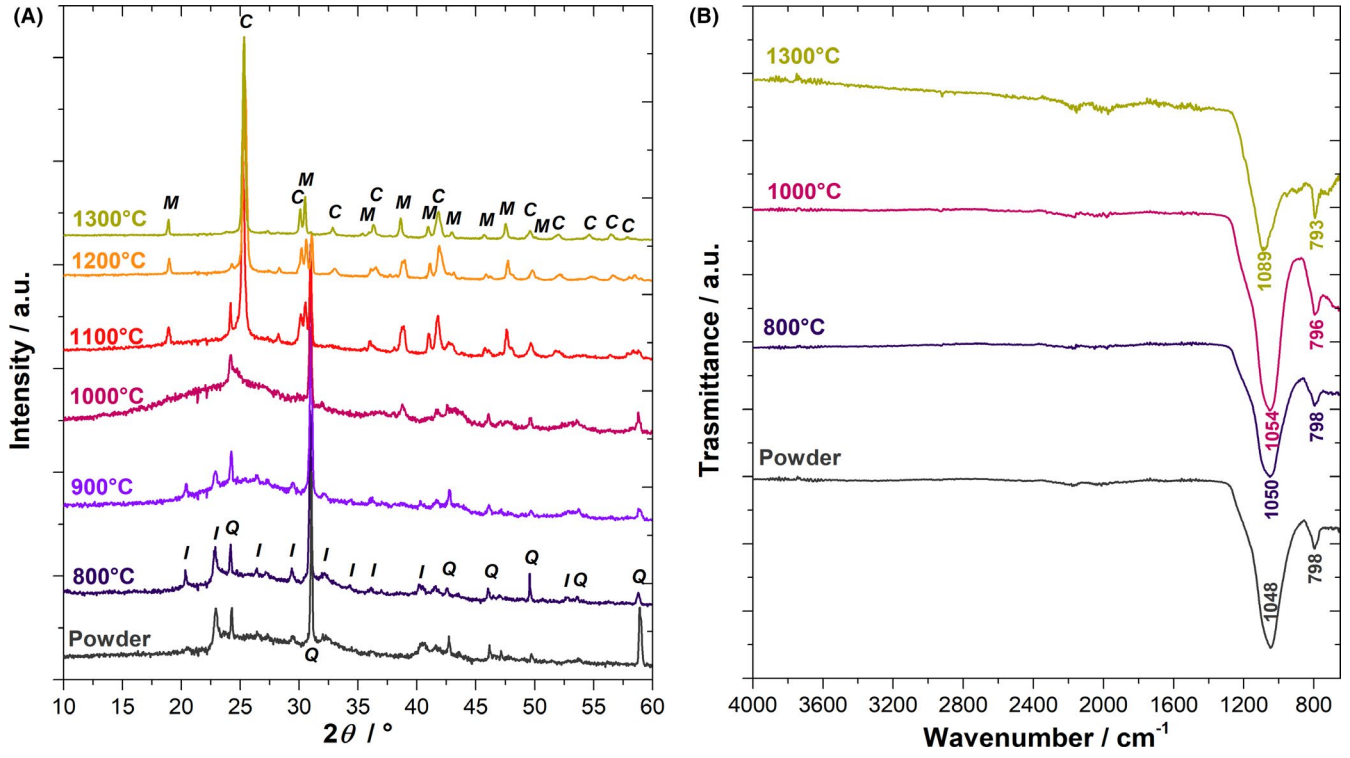

FIGURE 4 (A) X-ray diffraction diagrams and (B) Fourier transform infrared spectra of the raw material and cold sintering process samples. The phases in (A) are identified as: M = mullite, Q = quartz, I = illite [Color figure can be viewed at wileyonlinelibrary.com]

vitreous phase causing a reduction of the amorphous feature at $2\theta \approx 25°$. Finally, at 1300°C, the material is almost fully crystalline, characterized mainly by the presence of cristobalite and mullite. The crystallization of mullite from aluminum-silicate glass is not particularly surprising as it is an equilibrium phase predicted by the SiO_2–Al_2O_3 phase diagram.[54] On the other hand, cristobalite is not the most stable SiO_2 polymorph in the considered temperature range, tridymite being more stable between below 1470°C.[54] However, it is usually reported that cristobalite preferentially crystallizes from silicate glasses even below 1400°C,[55–57] and this can be largely affected by the presence of even low amounts of alkalis.[58] Furthermore, the formation of cristobalite during high-temperature treatments of diatomaceous earth has already been abundantly documented in the literature.[59,60]

The FTIR spectra of conventionally sintered diatomite samples are reported in Figure 4B. No clear differences can be identified with respect to the raw powder, this pointing

out the presence of compounds containing Si–O and Al–O bonds. Only a slight blue-shift of the Si–O stretching signal (≈1050 cm^{-1}) is present and can be attributed to the decomposition of clay minerals[42]/crystallization of mullite.[61]

The influence of pressure on the bulk density of cold sintered samples is shown in Figure 5, with the effect of temperature and solvent concentration being also included. Bulk density increases with the applied pressure in all the tested conditions, because pressure provides an extra driving force for densification.[2,62] Considering samples obtained with 3-M NaOH water solution as transient liquid-phase, a dramatic gain in bulk density is obtained when the cold sintering occurs at 150°C rather than at RT. This evidence is verified independently from the pressure level and points out that the densification mechanism is thermally activated.

As expected, the alkaline solution concentration plays a relevant role in improving densification by cold sintering: at 150°C, comparable density levels are achieved employing distilled water (pH <7) or diluted NaOH solutions (0.1–0.5 M, pH ≈ 13), but moving toward higher NaOH concentrations (1–3 M, pH >14), a clear gain in bulk density is detected at any pressure value. Besides pressure, the synergy of temperature and solution concentration provides successful results in CSP: the densest sample was obtained with 3 M NaOH solution at 150°C under 300-MPa pressure. Its theoretical density was estimated as 2.28 ± 0.01 g cm^{-3} by He picnometry. Such density appears in agreement with the literature values for diatomites, which typically ranges between 2 and 2.66 g cm^{-3}.[33] On such bases, the relative density of the materials cold sintered at 150°C can exceed 90% of the theoretical one (300 MPa, 3-M NaOH). On the other hand, the relative density of the samples cold sintered at RT never exceeded 70%, suggesting that they remained in a sort of "green" state.

To further confirm diatomite densification by cold sintering, Hg porosimetry was carried out on the densest CSP sample and on the loose diatomite powder for comparison. The cumulative pore volume distribution is reported in Figure 6. The results confirm the porous nature of diatomite, which contains pores ranging from the mesoscale to the macroscale. The total porosity is ≈0.65 cm^3 g^{-1}, which corresponds to about 60 vol% (assuming the density of the solid ≈2.3 g cm^{-3}). About 50% of the pore volume is above 800 nm, whereas the mesopores (<50 nm) account for 12% of the pore volume (0.077 cm^3 g^{-1}). After CSP (150°C, 300 MPa, 3-M NaOH), the structure is clearly densified and the pore volume drops to 0.046 cm^3 g^{-1}. Such reduction is particularly significant because the green body is expected to possess a porosity much larger than that measured on the loose diatomite powder. In fact, the sample in the green state contains both intragrains (measured by porosimetry on diatomite powder) and intergrains porosity (typically 50% of the green volume). Hence, Figure 6 reveals that CSP allows to remove not only the intergrains porosity but also the largest part of the "native" pores within the diatomite powder.

Using the bulk density calculated by He picnometry and the Hg porosimetry results, we can estimate that the porosity after CSP is below 10 vol%, this being in good agreement with the density measurements. Interestingly, after CSP, almost all the residual pores are in the mesoscale. This is quite unusual because in conventional sintering processes, densification proceeds starting from the smallest pores, and as such, during consolidation, the average pore size progressively increases. Upon CSP, the opposite behavior is observed. The origin of the phenomenon is not completely clear and

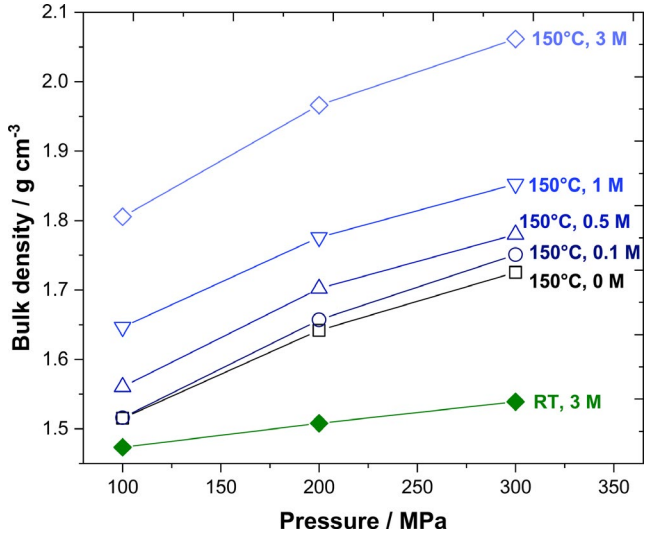

FIGURE 5 Bulk density evolution as a function of sintering temperature and solution concentration [Color figure can be viewed at wileyonlinelibrary.com]

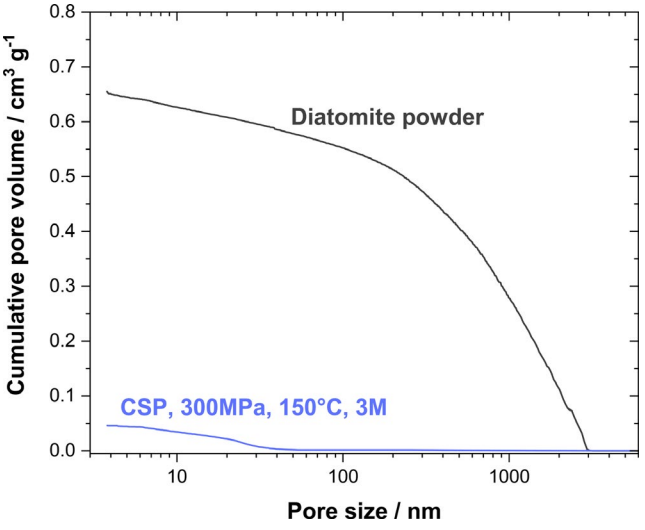

FIGURE 6 Cumulative pore volume measured by Hg porosimetry on loose diatomite powder and on the densest cold sintering process sample [Color figure can be viewed at wileyonlinelibrary.com]

deserves further investigation; in any case, we can point out that in CSP, the driving force for densification is the external pressure, whereas in conventional sintering, mass transport is driven by capillarity. Because capillarity pressures are proportional to the curvature, the smallest pores are more prone to densification; on the other hand, this effect is not expected in CSP. Moreover, we can speculate that water could be preferentially retained within the small pores, and being incompressible, it could somehow stabilize the mesopores. A definitive conclusion on the mechanisms cannot be drawn at the present stage, but the results suggest that CSP allows to obtain microstructure with unusual pore distribution.

The microstructure of CSP samples is shown in Figure 7 (fresh fracture surfaces). In all the pellets, a deformation of the starting powder is visible, the effect being more evident in samples pressed under 300 MPa. Powder deformation is also promoted in warm conditions; one can observe that the grains appear "flattened" after the CSP and oriented orthogonally to the pressure direction (top-bottom in Figure 7). The clear grain flattening points out that the main driving force of the process is the external pressure application (i.e., capillarity pressure being isotropic).

The microstructure of the cold sintered samples (150°C, 300 MPa, 3-M NaOH solution) shows good stability upon heating. In fact, the samples post-annealed at 800°C did not show substantial microstructural changes: their density remains constant (Table 1) and the fracture surface (Figure 8) shows flattened and oriented grains (like for nonannealed samples). The absence of significant densification upon heating confirms once more the good level of consolidation of the cold sintered material and proves that it can be employed also in applications at relatively high temperatures.

For the conventionally sintered samples, the bulk density increases from 1.2 to 2.2 g cm^{-3} between 800 and 1300°C (Figure 9). On the other hand, apparent density remains constant up to 1000°C suggesting that there is no close porosity formation in this temperature range. Then, it increases between 1000°C and 1100°C as a result of the partial crystallization of mullite and cristobalite (Figure 4A). It finally decreases at a higher temperature (despite crystallization proceeds) because of the transition from open to closed porosity.

The microstructure of samples treated at a temperature below 1000°C does not change significantly, and some frustule relicts are well visible (Figure 10). At 1100°C, an initial interconnected structure appears, which is even more appreciable at 1200 and 1300°C. Porosity evolves starting from 1100°C, and pores start to be closed, isolated, and rounded in shape by increasing the sintering temperature. Comparing the results in Figures 5 and 9, we can conclude that the densification achieved in CSP (300 MPa, 150°C, 3-M NaOH solution) can be reproduced by conventional sintering only at temperatures exceeding 1200°C. Therefore, CSP allows a downward shift in the consolidation temperature for diatomite of more than 1000°C.

Table 1 reports the equibiaxial flexural strength of the cold sintered material (150°C, 300 MPa, 3-M NaOH

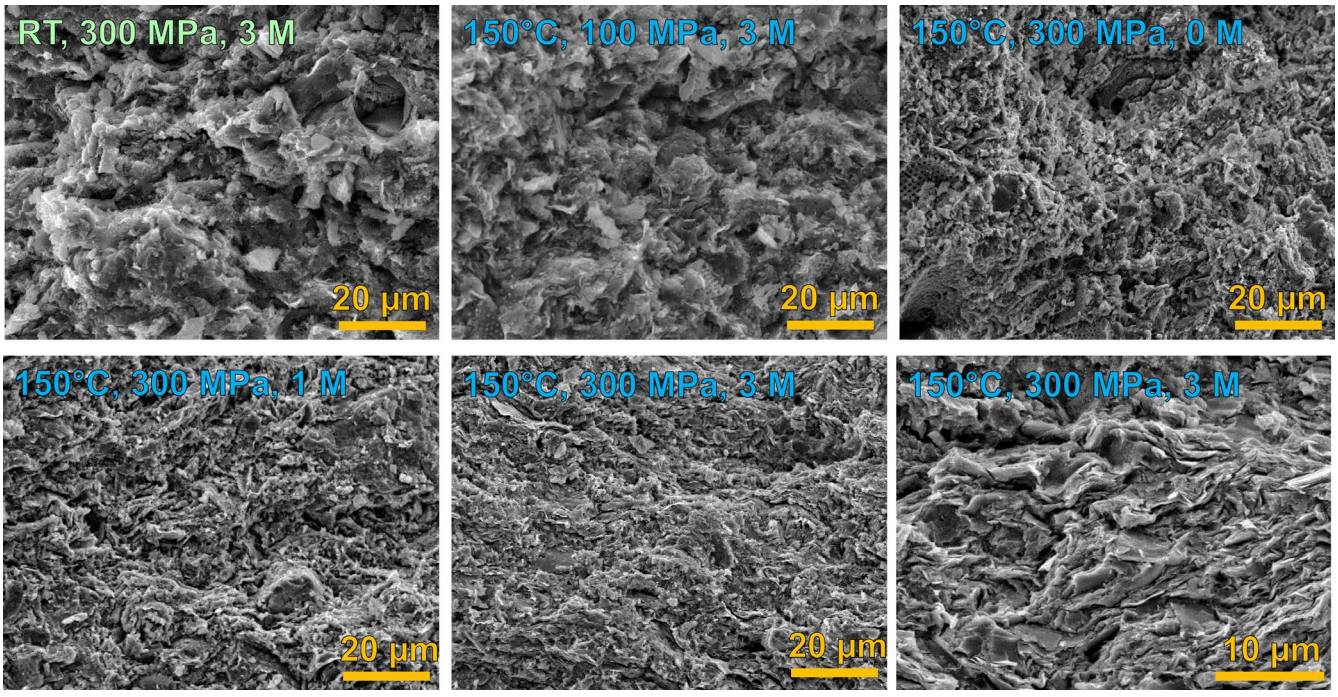

FIGURE 7 Scanning electron microscopy micrographs of the fresh fracture surfaces of cold sintered diatomite. The uniaxial pressure was applied along the top-bottom direction. Cold sintering process temperature and pressure are reported along with the NaOH solution concentration [Color figure can be viewed at wileyonlinelibrary.com]

	CSP	CSP + annealing at 800°C	Conventional sintering at 800°C
Bulk density (g cm^{-3})	2.06 ± 0.01	2.03 ± 0.01	1.22 ± 0.02
Flexural strength (MPa)	41.9 ± 3.8	79.1 ± 5.1	1.0 ± 0.3

TABLE 1 Bulk density (geometrical method), and biaxial flexural measured on the samples cold sintered at 150°C using 3 M NaOH solution and 300 MPa before and after annealing at 800°C

The properties of the samples conventionally sintered at 800°C are reported for comparison. The error corresponds to the standard deviation.

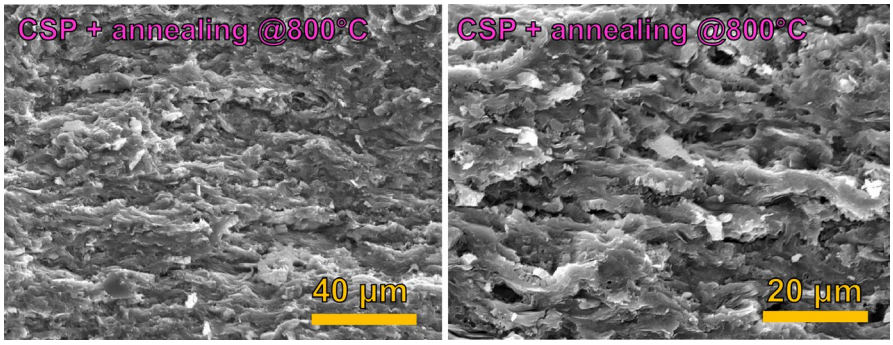

FIGURE 8 Scanning electron microscopy micrographs of fresh fracture surfaces of cold sintered diatomite (150°C, 300 MPa, 3 M NaOH solution) post-annealed at 800°C. The uniaxial pressure was applied along the top-bottom direction [Color figure can be viewed at wileyonlinelibrary.com]

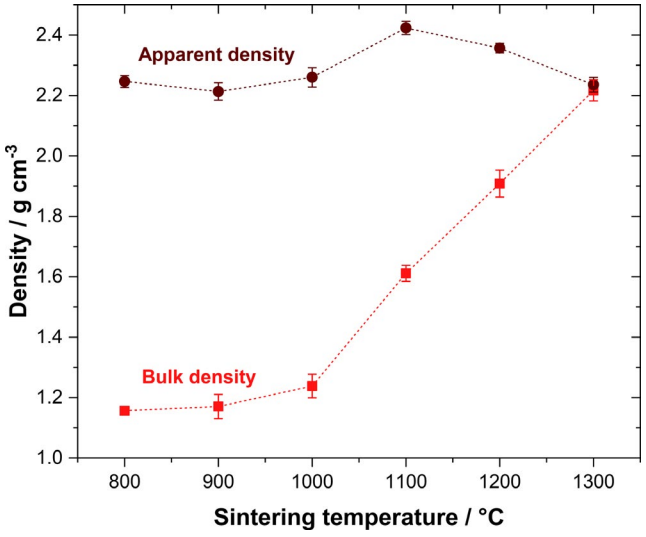

FIGURE 9 Bulk and apparent density as a function of the sintering temperature [Color figure can be viewed at wileyonlinelibrary.com]

solution) before and after post-annealing at 800°C. The material just after CSP possesses a mechanical resistance exceeding 40 MPa, which increases up to ≈80 MPa after annealing at 800°C. This value is lower than that reported by Akhtar et al. (about 100 MPa)[63] on ≈75% dense diatomite, although the latter was measured in compression, thus being definitely larger than the flexural one. In any case, the properties of cold sintered diatomite appear consistent with a properly sintered material where primary chemical bonds between particles develop. Cold sintered diatomite does not appear therefore as a "simple assembly of deformed particles" without effective interparticle bonding but behaves like a truly sintered artifact. For comparison, the mechanical strength of a conventionally pressed material annealed at 800°C is about 1 MPa, that is, ≈1/40 that obtained by CSP at nearly RT.

As previously pointed out, the densest CSP sample is obtained with 3 M NaOH solution at 150°C under 300 MPa pressure. Figure 11A shows the density evolution as a function of time for such material (time was assumed equal to zero when the sintering temperature was reached in the case of the specimens treated at 150°C or when the maximum pressure was achieved in the case of the samples processed at RT). One can observe that remarkable densification occurs in the isothermal stage at 150°C, this pointing out that sintering is not completed during the heating ramp. The densification rate (i.e., the slope of the curves) progressively decreases with time in warm conditions, and the density curves become substantially flat after about 5 min at 150°C. On the other hand, densification at RT is substantially completed in the first minute after the pressure application. This result is opposite to the expected one because the solvent concentration remains high during the entire process at RT, whereas most of the liquid is supposed to evaporate quickly at high temperatures. Therefore, one would expect that at 150°C, the decay of the sintering rate is faster than at RT. The almost "instantaneous" densification and the limited densification level (<70%) suggest that at RT, the samples substantially remain in a sort of green state, whereas proper sintering occurs at 150°C.

The densification mechanisms taking place during CSP at 150°C were investigated considering how the normalized densification rate $\left(\frac{1}{\rho}\frac{d\rho}{dt}\right)$ varies with the applied pressure (p_a).[11,62] In CSP, a uniaxial pressure is applied, similarly to the well-studied hot pressing systems; therefore, we can extend the models applied to hot pressing to CSP following the approach first suggested by Gonzalez-Julian et al.[11] The

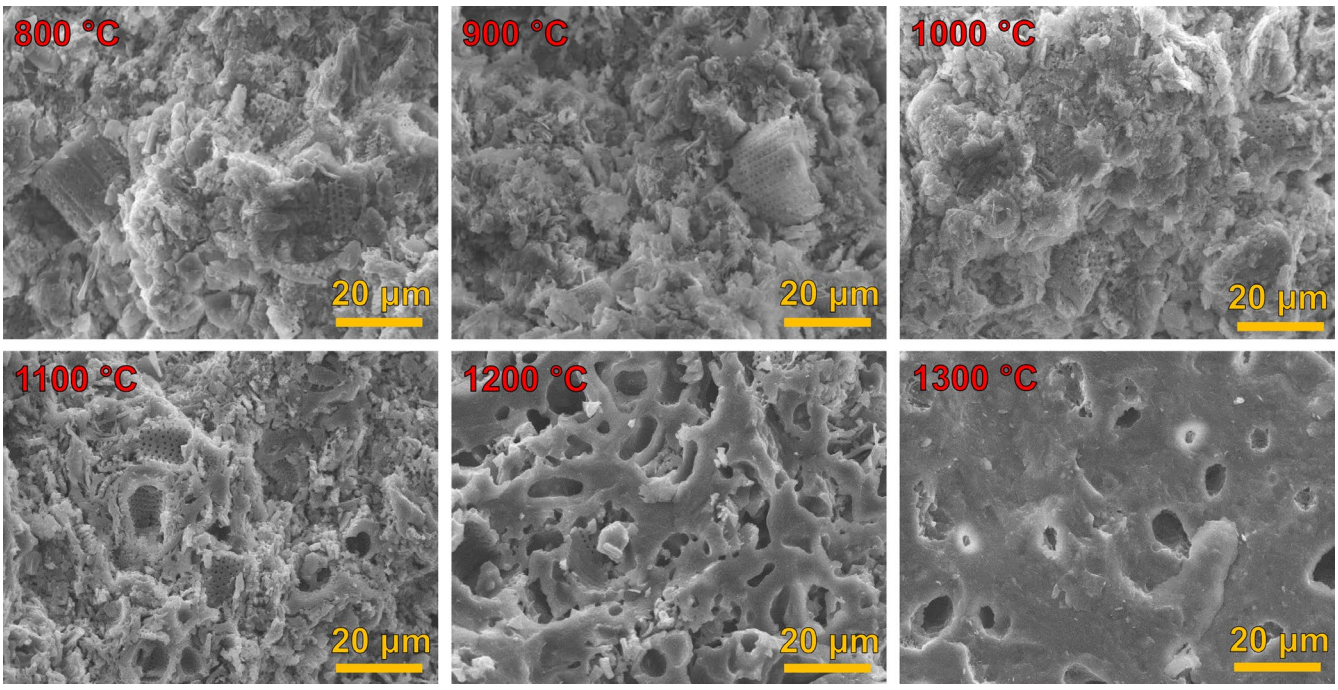

FIGURE 10 Scanning electron microscopy micrographs of the fresh fracture surfaces of conventionally sintered diatomite at different temperatures [Color figure can be viewed at wileyonlinelibrary.com]

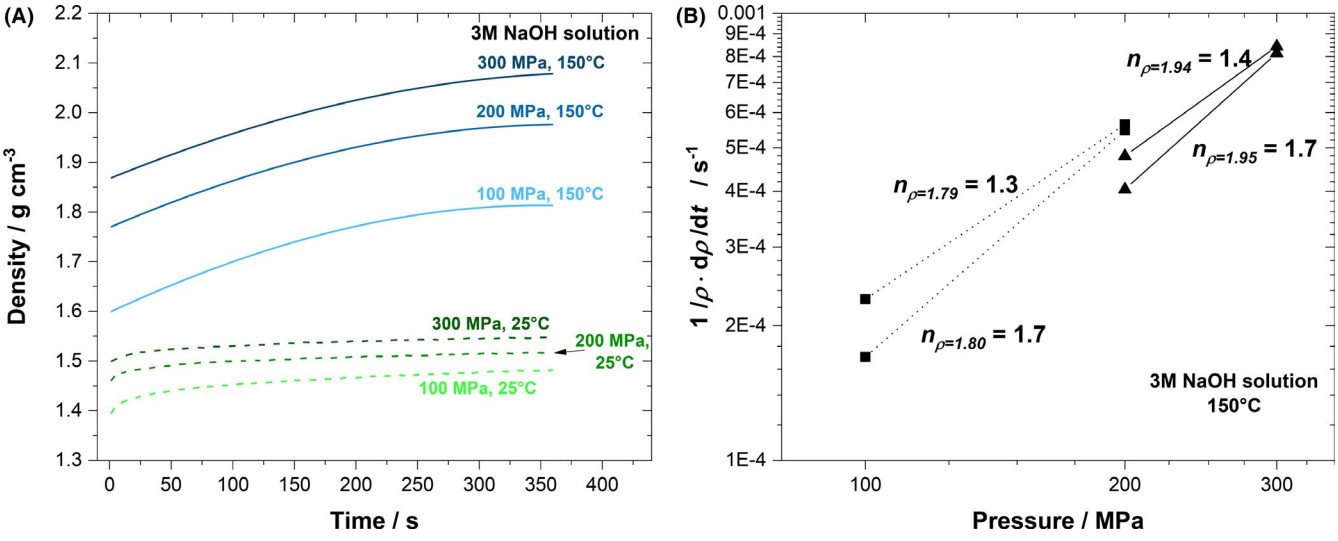

FIGURE 11 (A) Density evolution as a function of time in the case of cold sintering with 3 M NaOH solution at room temperature (dashed lines) and 150°C (solid lines); (B) strain rate as a function of the applied compaction pressure, considering different density values, for the samples treated at 150°C. Time = 0 s is assumed when the system reaches the sintering temperature (i.e., 150°C) [Color figure can be viewed at wileyonlinelibrary.com]

sintering constitutive equation during hot pressing can be written as:[62]

$$\frac{1}{\rho}\frac{d\rho}{dt} = \frac{HD\Phi^n}{G^m kT} p_a^n, \tag{2}$$

where H is a mechanism-dependent constant, D the diffusion coefficient of the rate-controlling species, Φ the stress intensity factor (which accounts for the pressure concentration in the neck region), G the particle size, T the absolute temperature, k the Boltzmann constant, m, and n being characteristic values depending on the densification mechanisms.

If the temperature is constant and the microstructure is a function of density only (i.e., grain size and Φ depend only on density), Equation (2) can be reduced to

$$\log\left(\frac{1}{\rho}\frac{d\rho}{dt}\right) \propto n \log p_a. \tag{3}$$

Therefore, the slope of the $\log\left(\frac{1}{\rho}\frac{d\rho}{dt}\right)$ versus $\log p_a$ plot, at a given value of p, represents the mechanism-dependent constant, n. As for the density evolution with time in Figure 11A, two values were considered, 1.79–1.80 g cm^{-3} and 1.94–1.95 g cm^{-3} for applied pressures equal to 100–200 MPa and 200–300 MPa, respectively. The resulting stress exponent ranges between 1.3 and 1.7, as shown in Figure 11B. From the literature, n should be equal to 1 in the case of liquid phase and viscous flow sintering; it is expected to be 1 or 2 in case of grain boundary sliding and larger than 3 in case of plastic deformation. Our results seem to exclude only plastic flow-assisted densification, which was recognized as dominant in other ceramic systems like ZnO.[11] On the other hand, the calculated exponents do not perfectly match neither with grain sliding nor with viscous flow or dissolution/reprecipitation. The strong relation between densification and caustic environments appears to support the idea that consolidation is driven by dissolution/reprecipitation, being silica solubility strongly related to pH.[46] Nevertheless, the final microstructures shown in Figure 6 seem more consistent with a viscous deformation of the grains that appear completely flattened after the treatment. A definitive conclusion on the densification mechanisms cannot be drawn at this point, but the results shown here suggest a complex behavior where more than one mass transport mechanism is activated simultaneously.

4 | CONCLUSIONS

The applicability of cold sintering to diatomaceous earth was explored. Diatomite powder can be densified above 90% of the theoretical density when the process is carried out at 150°C under 300 MPa in a caustic environment (3-M NaOH water solution). Such density value is similar to those achieved by conventional sintering at 1200–1300°C.

Despite the comparable density values, the microstructure of cold sintered samples differs from the conventionally fired materials. During cold sintering, the powder undergoes a substantial deformation promoted by the presence of the liquid phase and external pressure application. Moreover, the initial phase composition (quartz, glass, and illite) is maintained after sintering upon CSP, whereas an evident reorganization occurs upon traditional firing with the formation of mullite and cristobalite.

The bending strength of cold sintered diatomite exceeds 40 MPa, confirming that cold sintering leads to a "properly sintered artifact" with strong interparticle bonding. The failure stress can be increased up to ≈80 MPa after post-annealing at 800°C, whereas conventionally pressed samples sintered at 800°C fail under ≈1 MPa.

ACKNOWLEDGMENTS

Mr. L. Zottele, Ms. A. Conci, Ms. C. Gavazza, Dr. F. Valentini, Prof. D. Maniglio, and Prof. A. Pegoretti (DII, University of Trento) are warmly acknowledged for the help and contribution. This work is supported by the Italian Ministry of University and Research (MIUR) within the "Departments of Excellence" (DII, University of Trento). M. Biesuz, G. D. Sorarù, and V.M. Sglavo acknowledge the support from the MIUR within the programs PRIN2017—2017FCFYHK "DIRECTBIOPOWER" and PRIN2017—2017PMR932 "Nanostructured Porous Ceramics for Environmental and Energy Applications".

ORCID

Enrico Giust https://orcid.org/0000-0002-3945-3846
Gian D. Sorarù https://orcid.org/0000-0002-0453-3379
Vincenzo M. Sglavo https://orcid.org/0000-0001-9133-7204
Mattia Biesuz https://orcid.org/0000-0002-4338-4177

REFERENCES

1. Sohrabi Baba Heidary D, Lanagan M, Randall CA. Contrasting energy efficiency in various ceramic sintering processes. J Eur Ceram Soc. 2018;38(4):1018–29.
2. Biesuz M, Grasso S, Sglavo VM. What's new in ceramics sintering? A short report on the latest trends and future prospects. Curr Opin Solid State Mater Sci. 2020;24(5):100868.
3. Guo J, Guo H, Baker AL, Lanagan MT, Kupp ER, Messing GL, et al. Cold sintering: a paradigm shift for processing and integration of ceramics. Angew Chemie, Int Ed. 2016;55(38):11457–61.
4. Grasso S, Biesuz M, Zoli L, Taveri G, Duff AI, Ke D, et al. A review of cold sintering processes. Adv Appl Ceram. 2020;119(3):115–43.
5. Vakifahmetoglu C, Karacasulu L. Cold sintering of ceramics and glasses: a review. Curr Opin Solid State Mater Sci. 2020;24(1):100807.
6. Guo J, Floyd R, Lowum S, Maria JP, Herisson de Beauvoir T, Seo JH, et al. Cold sintering: progress, challenges, and future opportunities. Annu Rev Mater Res. 2019;49(1):275–95.
7. Ibn-Mohammed T, Randall CA, Mustapha KB, Guo J, Walker J, Berbano S, et al. Decarbonising ceramic manufacturing: a techno-economic analysis of energy efficient sintering technologies in the functional materials sector. J Eur Ceram Soc. 2019;39(16):5213–35.
8. Yanagisawa K, Kanahara S, Nishioka M, Yamasaki N. Immobilization of radioactive wastes in hydrothermal synthetic rock, (II). J Nucl Sci Technol. 1984;21(7):558–60.
9. Yanagisawa K, Nishioka M, Yamasaki N. Immobilization of cesium into pollucite structure by hydrothermal hot-pressing. J Nucl Sci Technol. 1987;24(1):51–60.
10. Yamasaki N, Kai T, Nishioka M, Yanagisawa K, Ioku K. Porous hydroxyapatite ceramics prepared by hydrothermal hot-pressing. J Mater Sci Lett. 1990;9(10):1150–1.
11. Gonzalez-Julian J, Neuhaus K, Bernemann M, da Silva JP, Laptev A, Bram M, et al. Unveiling the mechanisms of cold sintering of ZnO at 250°C by varying applied stress and characterizing grain boundaries by Kelvin Probe Force Microscopy. Acta Mater. 2018;144:116–28.
12. Biesuz M, Taveri G, Duff AI, Olevsky E, Zhu D, Hu C, et al. A theoretical analysis of cold sintering. Adv Appl Ceram. 2020;119(2):75–89.

13. Wang D, Tsuji K, Randall CA, Trolier-McKinstry S. Model for the cold sintering of lead zirconate titanate ceramic composites. J Am Ceram Soc. 2020;103(9):4894–902.
14. Shen H, Guo N, Zhao L, Shen P. Role of ion substitution and lattice water in the densification of cold-sintered hydroxyapatite. Scr Mater. 2020;177:141–5.
15. Karacasulu L, Ogur E, Piskin C, Vakifahmetoglu C. Cold sintering of soda-lime glass. Scr Mater. 2021;192:111–4.
16. Guo H, Baker A, Guo J, Randall CA. Cold sintering process: a novel technique for low-temperature ceramic processing of ferroelectrics. J Am Ceram Soc. 2016;99(11):3489–507.
17. Van BW. Lead-free piezoceramics. Nature. 2004;432:84–7.
18. Jo W, Daniels JE, Jones JL, Tan X, Thomas PA, Damjanovic D, et al. Evolving morphotropic phase boundary in lead-free ($Bi_{1/2}$ $Na_{1/2}$)TiO_3–$BaTiO_3$ piezoceramics. J Appl Phys. 2011;109:014110.
19. Karacasulu L, Tokkan M, Bortolotti M, Ischia G, Adem U, Vakifahmetoglu C. Electrical characteristics of low temperature densified barium titanate. Ceram Int. 2020;46(10):16670–6.
20. Chen N, Xiao B, Xu X, Sun T, Chen M, Hu R, et al. Cold-sintered $Ni_{0.2}Cu_{0.2}Zn_{0.6}Fe_2O_4$-$Li_2MoO_4$ ceramic composites with enhanced magnetodielectric properties. J Eur Ceram Soc. 2021;41:1310–6.
21. Serrano A, Caballero-Calero O, García MÁ, Lazić S, Carmona N, Castro GR, et al. Cold sintering process of ZnO ceramics: effect of the nanoparticle/microparticle ratio. J Eur Ceram Soc. 2020;40(15):5535–42.
22. Funahashi S, Guo J, Guo H, Wang KE, Baker AL, Shiratsuyu K, et al. Demonstration of the cold sintering process study for the densification and grain growth of ZnO ceramics. J Am Ceram Soc. 2017;100(2):546–53.
23. Kang X, Floyd R, Lowum S, Cabral M, Dickey E, Maria J-P. Mechanism studies of hydrothermal cold sintering of zinc oxide at near room temperature. J Am Ceram Soc. 2019;102:4459–69.
24. Hérisson de Beauvoir T, Estournès C. Translucent γ-AlOOH and γ-Al_2O_3 glass-ceramics using the cold sintering process. Scr Mater. 2021;194:113650.
25. Kabir A, Espineira-Cachaza M, Fiordaliso EM, Ke D, Grasso S, Merle B, et al. Effect of cold sintering process (CSP) on the electro-chemo-mechanical properties of Gd-doped ceria (GDC). J Eur Ceram Soc. 2020;40(15):5612–8.
26. Charoonsuk T, Sukkha U, Kolodiazhnyi T, Vittayakorn N. Enhancing the densification of ceria ceramic at low temperature via the cold sintering assisted two-step sintering process. Ceram Int. 2018;44:S54–S57.
27. Elissalde C, Chung U-C, Josse M, Goglio G, Suchomel MR, Majimel J, et al. Single-step sintering of zirconia ceramics using hydroxide precursors and Spark Plasma Sintering below 400°C. Scr Mater. 2019;168:134–8.
28. Ndayishimiye A, Largeteau A, Prakasam M, Pechev S, Dourges MA, Goglio G. Low temperature hydrothermal sintering process for the quasi-complete densification of nanometric α-quartz. Scr Mater. 2018;145:118–21.
29. Ndayishimiye A, Tsuji K, Wang K, Bang SH, Randall CA. Sintering mechanisms and dielectric properties of cold sintered (1–*x*)SiO_2–*x*PTFE composites. J Eur Ceram Soc. 2019;39(15):4743–51.
30. Ke D, Jiang A, Biesuz M, Bortolotti M, Taveri G, Wang X, et al. Ultra-low energy joining: an invisible strong bond at room temperature. J Eur Ceram Soc. 2019;39(16):5358–63.
31. Taveri G, Grasso S, Gucci F, Tousek J, Dlouhy I. Bio-inspired hydro-pressure consolidation of silica. Adv Funct Mater. 2018;28:1805794.
32. Bouville F, Studart AR. Geologically-inspired strong bulk ceramics made with water at room temperature. Nat Commun. 2017;8:14655.
33. Ivanov SÉ, Belyakov AV. Diatomite and its applications. Glas Ceram. 2008;65(1–2):48–51.
34. Gordon R, Losic D, Tiffany MA, Nagy SS, Sterrenburg FAS. The Glass Menagerie: diatoms for novel applications in nanotechnology. Trends Biotechnol. 2009;27(2):116–27.
35. Maher S, Kumeria T, Aw MS, Losic D. Diatom silica for biomedical applications: recent progress and advances. Adv Healthc Mater. 2018;7(19):1800552.
36. Loganina VI, Simonov EE, Jezierski W, Małaszkiewicz D. Application of activated diatomite for dry lime mixes. Constr Build Mater. 2014;65:29–37.
37. Zhao Y, Tian G, Duan X, Liang X, Meng J, Liang J. Environmental applications of diatomite minerals in removing heavy metals from water. Ind Eng Chem Res. 2019;58(27):11638–52.
38. Korunic Z. *Review*Diatomaceous earths, a group of natural insecticides. J Stored Prod Res. 1998;34(2–3):87–97.
39. Huang CW, Hsueh CH. Piston-on-three-ball versus piston-on-ring in evaluating the biaxial strength of dental ceramics. Dent Mater. 2011;27(6):e117–e123.
40. Gong J, Miao H, Peng Z. On the contact area for nanoindentation tests with Berkovich indenter: case study on soda-lime glass. Mater Lett. 2004;58(7–8):1349–53.
41. Ilia I, Stamatakis M, Perraki T. Mineralogy and technical properties of clayey diatomites from north and central Greece. Open Geosci. 2009;1(4): 393–403.
42. Mohammed J, Nasri NS, Ahmad Zaini MA, Hamza UD, Ani FN. Adsorption of benzene and toluene onto KOH activated coconut shell based carbon treated with NH_3. Int Biodeterior Biodegradation. 2015;102:245–55.
43. Socrates G. Infrared and Raman characteristic group frequencies: tables and charts. 3rd ed. Chichester: John Wiley & Sons, Ltd.; 2004.
44. Al-Oweini R, El-Rassy H. Synthesis and characterization by FTIR spectroscopy of silica aerogels prepared using several $Si(OR)_4$ and $R''Si(OR')_3$ precursors. J Mol Struct. 2009;919(1–3):140–5.
45. Nefzi H, Abderrabba M, Ayadi S, Labidi J. Formation of palygorskite clay from treated diatomite and its application for the removal of heavy metals from aqueous solution. Water. 2018;10(9):1257.
46. Doremus RH. Glass science. II; New York, NY: John Wiley & Sons, Inc.; 1994.
47. Crundwell FK. On the mechanism of the dissolution of quartz and silica in aqueous solutions. ACS Omega. 2017;2(3):1116–27.
48. Bang SH, Tsuji K, Ndayishimiye A, Dursun S, Seo J-H, Otieno S, et al. Toward a size scale-up cold sintering process at reduced uniaxial pressure. J Am Ceram Soc. 2020;103(4):2322–7.
49. Garnica-Romo MG, Yañez-Limón JM, Villicaña M, Pérez-Robles JF, Zamorano-Ulloa R, González-Hernandez J. Structural evolution of sol–gel SiO_2 heated glasses containing silver particles. J Phys Chem Solids. 2004;65(6):1045–52.
50. Mielenz RC. Thermogravimetric analysis of clay and clay-like minerals. Clays Clay Miner. 1953;2(1):285–314.
51. de Araújo JH, da Silva NF, Acchar W, Gomes UU. Thermal decomposition of illite. Mater Res. 2004;7(2):359–61.
52. Muller F. Structural transformation of 2:1 dioctahedral layer silicates during dehydroxylation-rehydroxylation reactions. Clays Clay Miner. 2000;48(5):572–85.
53. Gualtieri AF, Ferrari S. Kinetics of illite dehydroxylation. Phys Chem Miner. 2006;33(7):490–501.

54. Carter CB, Norton MG. Ceramic materials science and engineering. New York, NY: Springer; 2007.
55. Mazurin OV, Leko VK, Komarova LA. Crystallization of silica and titanium oxide-silica corning glasses (codes 7940 and 7971). J Non Cryst Solids. 1975;18(1):1–9.
56. Li X, Yin X, Zhang L, He S. The devitrification kinetics of silica powder heat-treated in different conditions. J Non Cryst Solids. 2008;354(28):3254–9.
57. Wagstaff FE. Crystallization kinetics of internally nucleated vitreous silica. J Am Ceram Soc. 1968;51(8):449–53.
58. Dapiaggi M, Pagliari L, Pavese A, Sciascia L, Merli M, Francescon F. The formation of silica high temperature polymorphs from quartz: influence of grain size and mineralising agents. J Eur Ceram Soc. 2015;35(16):4547–55.
59. Zhang X, Liu X, Meng G. Sintering kinetics of porous ceramics from natural diatomite. J Am Ceram Soc. 2005;88(7):1826–30.
60. Akhtar F, Vasiliev PO, Bergström L. Hierarchically porous ceramics from diatomite powders by pulsed current processing. J Am Ceram Soc. 2009;92(2):338–43.
61. Song K, Kim W, Suh C-Y, Bang J-H, Ahn J-W. Preparation of mullite-silica composites using silica-rich monophasic precursor obtained as a byproduct of mineral carbonation of blast-furnace slag. Minerals. 2018;8(5):219.
62. Rahaman MN. Ceramic processing and sintering. New York, USA: Marcel Dekker; 1996.
63. Akhtar F, Rehman Y, Bergström L. A study of the sintering of diatomaceous earth to produce porous ceramic monoliths with bimodal porosity and high strength. Powder Technol. 2010;201(3):253–7.

How to cite this article: Galotta A, Giust E, Bortolotti M, Sorarù GD, Sglavo VM, Biesuz M. Cold sintering of diatomaceous earth. *J Am Ceram Soc*. 2021;104:4329–4340. https://doi.org/10.1111/jace.17863